Phase-Informed Discontinuous Galerkin Method for Extremely High-Frequency Wave Modeling

Haoqiang Feng, *Graduate Student Member, IEEE*, Jianping Huang, Caipin Li, Kang Liu, Yi-Yao Wang, *Graduate Student Member, IEEE*, Wei E. I. Sha, *Senior Member, IEEE*, and Qiwei Zhan, *Member, IEEE*

***Abstract*— Two long-standing problems exist in the high-frequency electromagnetic scattering analysis: 1) full-wave methods suffer a geometric increase in computational costs, along with the rising frequencies and 2) ray tracing methods struggle to acquire sufficient phase information when dealing with complex targets. To address these two issues, we propose a phase-informed hybridizable discontinuous Galerkin (PI-HDG) method for extremely high-frequency modeling. Similar to the physics-informed machine learning algorithms, we integrate the prior knowledge of phase information into the basis-function construction in the PI-HDG algorithm, thus combining both strengths from the HDG method and geometric optics ansatz. Numerical experiments show that the PI-HDG algorithm can accurately compute high-frequency scattering characteristics of complex targets. Specifically, in a multiple scattering scenario, we achieve only 1/10 temporal consumption while 1/16 for the memory, when compared with the reference finite-element software.**

***Index Terms*— Discontinuous Galerkin (DG) method, Helmholtz equation, high frequency, numerical discretization scheme, phase information.**

I. Introduction

NUMERICAL modeling for electromagnetic scattering characteristics plays an indispensable role in the realms of antenna design [1], microwave imaging [2], and wireless communication [3]. Full-wave numerical methods typically require around 10–20 sampling points per wavelength (PPWs) [4] to ensure sufficient precision. The degrees of freedom (DoFs) are around $\mathcal{O}(k^d)$, where k is the wavenumber and d is the ambient dimension. Moreover, the computational complexity of the global system is about $\mathcal{O}(k^{3d/2})$ to $\mathcal{O}(k^{2d})$. Therefore, these approaches encounter substantial computational demands, especially in the high-frequency modeling. Nonetheless, even with a constant PPW, the error of numerical results worsens as k increases. This extra k-dependent error, known as the pollution error, further exacerbates the dilemma in full-wave modeling [5], [6], [7].

Several alternative full-wave approaches have been proposed to reduce the pollution effect, including the generalized finite-element method [8], the continuous interior-penalty finite-element method [9], and the interpolated optimized finite-difference method [10]. These methods either impose stricter conditions on mesh size or entail a k-dependent polynomial approximation degree. On the other hand, the discontinuous Galerkin (DG) method segregates the entire computational domain into individual elements, treating each one as a separate domain. This algorithm boasts exceptional characteristics, such as high-order accuracy, scalability, versatility, and robustness. Consequently, the DG method has been effectively employed in applications for a variety of multiscale and multiphysics problems, including anisotropic poroelastic, elastic, fluid media [11], [12], [13], and electromagnetic waves [14], [15], [16]. Moreover, Cockburn and coworkers [17], [18] introduce the hybridizable DG (HDG) method to reduce the unknowns further. Notably, [19] demonstrates the preliminary capability of the HDG scheme to eliminate the pollution error for the Helmholtz equation.

Since, in the high-frequency region, the nature of wave propagation behaves like rays, various methods employ ray theory to address the Helmholtz equation. Ray tracing methods are a typical category of them, including geometrical optics, the physical theory of diffraction, and the shooting and bouncing ray methods. These approaches successfully solve electromagnetic scattering problems from complex objects [20], [21]. In addition, utilizing asymptotic expansion methods, a range of algorithms aim to incorporate plane waves into the full-wave basis functions, such as the partition of unity finite-element methods [22], virtual element methods [23], and ultraweak variational formulation [24]. However, the number of plane waves required is k-dependent. This tremendously increases the computational cost and

Manuscript received 26 January 2024; revised 26 May 2024; accepted 13 June 2024. Date of publication 18 July 2024; date of current version 9 August 2024. This work was supported in part by the National Key Research and Development Program of China under Grant 2022YFB3902400, in part by the National Natural Science Foundation of China under Grant 92066105, and in part by Zhejiang Provincial Natural Science Foundation of China under Grant LDT23F04014F01. *(Corresponding author: Qiwei Zhan.)*

Haoqiang Feng, Yi-Yao Wang, Wei E. I. Sha, and Qiwei Zhan are with the Key Laboratory of Advanced Micro/Nano Electronic Devices and Smart Systems of Zhejiang Province, Innovative Institute of Electromagnetic Information and Electronic Integration, College of Information Science and Electronic Engineering, Zhejiang University, Hangzhou 310058, China (e-mail: qwzhan@zju.edu.cn).

Jianping Huang is with the Geosciences Department, China University of Petroleum (East China), Qingdao, Shandong 266580, China, and also with the Pilot National Laboratory for Marine Science and Technology (Qingdao), Qingdao, Shandong 266000, China.

Caipin Li is with Xi'an Institute of Space Radio Technology, Xi'an 710071, China.

Kang Liu is with the College of Electronic Science and Technology, National University of Defense Technology, Changsha 410073, China.

Color versions of one or more figures in this article are available at https://doi.org/10.1109/TAP.2024.3427389.

Digital Object Identifier 10.1109/TAP.2024.3427389

induces severely ill-conditioned global systems owing to the linear-dependent basis functions [25].

It is noteworthy that scientific machine learning, integrating prior physical knowledge into neural networks, exhibits its superiority in real-time high-precision multiphysics modeling of large-scale electronic chips [26]. Similarly, in the geometric optics ansatz, phases and amplitudes are independent of the frequency and can be extracted a priori. This inspires us to incorporate this prior k-independent phase information into full-wave modeling. For instance, [27] acquires phase information by analytical formulation or solving the eikonal equation, subsequently incorporating these known phases into the basis functions. This phase-based method substantially enhances both stability and accuracy with very low PPW in typical cases [28]. Unfortunately, global phases computation for complex targets remains a challenging task. Alternatively, Fang et al. [29], [30] and Yeung et al. [31] acquire phase information from the full-wave solution in the relatively low-frequency region. This effectively enables its application in complex scenario modeling. However, the former may suffer from the pollution error due to the first-order basis function, while the latter employs the interior-penalty DG method, resulting in a larger number of DoFs.

Along this line, in this article, aiming at electromagnetic scattering applications in the extremely high-frequency region, we present a phase-informed hybridizable DG (PI-HDG) method. We enhance the basis functions by incorporating phase information from solutions in the relatively low-frequency region. These phase-informed basis functions effectively capture the oscillatory components of the Helmholtz equation solution. Therefore, the PI-HDG method demands fewer DoFs to achieve the equivalent accuracy.

The innovations delivered from this article are summarized as follows.

1) The PI-HDG method integrates the HDG methodology with a geometrical optics ansatz, continuing to leverage the superior accuracy and efficiency of the HDG method in high-frequency modeling.
2) We adopt a phase extraction technique to establish the relationship between wave fields in the low- and high-frequency regions. This enables us to obtain more comprehensive phase information, even when dealing with complex targets.
3) In the asymptotic expansion, we employ the gradient of phase (the wave propagation direction) rather than the phase itself. This effectively alleviates the problem posed by highly exponential oscillatory integrals.

This article is organized as follows. Section II elaborates the implementation details of the phase-informed HDG method for the Helmholtz equation. Section III shows numerical experiments, corroborating the stability, convergence, accuracy, and efficiency. Section IV gives conclusions.

II. Numerical Framework

A. Relationships Between the Maxwell's Equations and the Helmholtz Equation

It is well established that electromagnetic wave propagation problems in the frequency domain can be commonly expressed using time-harmonic Maxwell's equations as follows:

$$\begin{cases} \nabla \times \boldsymbol{E} = -j\omega\mu \boldsymbol{H} \\ \nabla \times \boldsymbol{H} = \boldsymbol{J} + j\omega\varepsilon \boldsymbol{E} \\ \nabla \cdot \varepsilon \boldsymbol{E} = \rho \\ \nabla \cdot \mu \boldsymbol{H} = 0 \end{cases} \tag{1}$$

where $\boldsymbol{E}$ and $\boldsymbol{H}$ represent the electric- and magnetic-field intensities, respectively; $\boldsymbol{J}$ stands for electric current density; ρ for electric charge density; ε and μ are the permittivity and permeability, respectively; j denotes the imaginary unit; and ω signifies the angular frequency.

In high-frequency modeling, the focus is primarily on Faraday's law and Ampere's law, which correspond to the first two equations within (1). The integration of Faraday's law with Ampere's law leads to

$$\nabla \times (\nabla \times \boldsymbol{E}) - \omega^2 \mu\varepsilon \boldsymbol{E} = -\mathrm{j}\omega\mu \boldsymbol{J}. \tag{2}$$

Equation (2) can be further expressed as follows:

$$\nabla(\nabla \cdot \boldsymbol{E}) \underbrace{-\nabla^2 \boldsymbol{E} - k^2 \boldsymbol{E} = \boldsymbol{f}}_{\text{Helmholtz equation}} \tag{3}$$

with the spatially dependent wavenumber k, where $k^2 = \omega^2\mu\varepsilon$ and $\boldsymbol{f}$ represents the source term. By neglecting the first term on the left-hand side, we derive the Helmholtz equation, which holds true in 2-D TE-wave scattering scenarios.

In Cartesian coordinates, each component of the electric-field intensity satisfies the scalar Helmholtz equation as follows:

$$-\Delta u - k^2 u = f \tag{4}$$

where u and f are one of the three components of the electric-field intensity and source term, respectively.

B. Asymptotic Expansions of the Helmholtz Equation

Classical direct algorithms face extremely high-computational costs in high-frequency modeling, while asymptotic methods, by analytically addressing the Helmholtz equation, exhibit superior effectiveness. The standard derivation of the geometric optics ansatz employs the Luneberg-Kline expansion [32, p. 93] to express the solution of the Helmholtz equation as follows:

$$u(\mathbf{x}) \sim e^{ik\varphi(\mathbf{x})} \sum_{\ell=0}^{\infty} \frac{A_\ell(\mathbf{x})}{k^\ell}. \tag{5}$$

By taking $k \to \infty$ and focusing solely on the first term, we obtain

$$u(\mathbf{x}) = A(\mathbf{x}) e^{ik\varphi(\mathbf{x})} + \mathcal{O}\left(\frac{1}{k}\right) \tag{6}$$

where $A(\mathbf{x})$ is the first term of $A_\ell(\mathbf{x})$, commonly referred to as the amplitude and $\varphi(\mathbf{x})$ as the phase. The essential characteristics of the geometric optics ansatz are as follows.

1) $A(\mathbf{x})$ and $\varphi(\mathbf{x})$ are independent of the wavenumber k.
2) $A(\mathbf{x})$ and $\varphi(\mathbf{x})$ depend on the medium material and the excitation source.

Nonetheless, a notable constraint of the asymptotic expansion (6) is its ability to capture single-phase wave fields. While, in general, the phase function $\varphi(\mathbf{x})$ and the amplitude function $A(\mathbf{x})$ are multivalued functions corresponding to multiple wavefront arrivals [33]. Consequently, the single-phase geometric optics ansatz (6) can be further deconstructed into a superposition of multiple wavefronts, taking the form

$$u(\mathbf{x}) = \sum_{n=1}^{N(\mathbf{x})} \left\{ A_n(\mathbf{x}) e^{ik\varphi_n(\mathbf{x})} \right\} + \mathcal{O}\left(\frac{1}{k}\right) \tag{7}$$

where $N(\mathbf{x})$ is the number of wavefronts, and the phases $\varphi_n(\mathbf{x})$ and amplitudes $A_n(\mathbf{x})$ are single-valued functions corresponding to the nth wavefront.

Note that (7) divides the solution into two components: the frequency-related component, denoted as k, and the frequency-independent components, denoted as $A_n(\mathbf{x})$ and $\varphi_n(\mathbf{x})$. Inspired by such characteristics, provided that we obtain the phases $\varphi_n(\mathbf{x})$ a priori, we can solely concentrate on the computation of the amplitudes $A_n(\mathbf{x})$. In addition, this method is more effective in the high-frequency region due to smaller asymptotic expansion errors, as shown in (7).

Based on the above geometric optics ansatz, we can derive a local plane wave approximation at any point. Indeed, using Taylor expansions on a small neighborhood around an observation point $\mathbf{x}_0$, we have

$$\begin{aligned} e^{ik\varphi_n(\mathbf{x})} &= e^{ik(\varphi_n(\mathbf{x}_0)+\nabla\varphi_n(\mathbf{x}_0)\cdot(\mathbf{x}-\mathbf{x}_0))} \\ &= e^{ik(\varphi_n(\mathbf{x}_0)-\nabla\varphi_n(\mathbf{x}_0)\mathbf{x}_0)} \cdot e^{ik\nabla\varphi_n(\mathbf{x}_0)\cdot\mathbf{x}}. \end{aligned} \tag{8}$$

Substituting (8) into (7), and neglecting the error term, we obtain

$$u(\mathbf{x}) = \sum_{n=1}^{N(\mathbf{x})} \left\{ B_n(\mathbf{x}) e^{ik\mu_n(\mathbf{x})} \right\} \tag{9}$$

with

$$\begin{aligned} B_n(\mathbf{x}) &= A_n(\mathbf{x}) e^{ik(\varphi_n(\mathbf{x}_0)-\nabla\varphi_n(\mathbf{x}_0)\mathbf{x}_0)} \\ \mu_n(\mathbf{x}) &= \nabla\varphi_n(\mathbf{x}_0)\cdot\mathbf{x} \end{aligned} \tag{10}$$

where $B_n(\mathbf{x})$ is the extended amplitude and $\mu_n(\mathbf{x})$ is the wave propagation direction of the nth ray at $\mathbf{x}_0$. Note that the subscript n is necessary to ensure $\mu_n(\mathbf{x})$ changes slowly, since the rays at $\mathbf{x}_0$ may diverge fast when near the source or in the multiple reflection scenario.

It is remarkable that in high-frequency modeling, due to (9), we inevitably have to compute highly oscillatory integrals involving exponential functions [34], [35]. In our subsequent procedures, (32) and (33) also encounter this issue. Fortunately, since we perform the local plane wave approximation, $\mu_n(\mathbf{x})$ can be considered to change slowly within a small neighborhood. This effectively alleviates the oscillations in integrals.

Based on the above analysis, we present the flowchart of the numerical framework, as shown in Fig. 1.

1) We first use the full-wave HDG method to compute the wave field $u(\mathbf{x})$ in the relatively low-frequency region, as detailed in Section II-C.

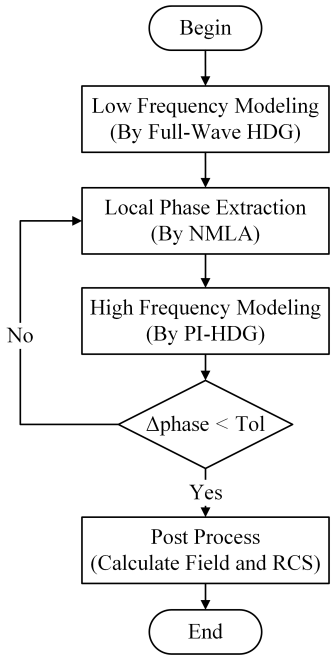

Fig. 1. Flowchart of the numerical framework.

2) Subsequently, we introduce the numerical microlocal analysis (NMLA) method to extract the wave propagation directions $\mu_n(\mathbf{x})$ from the full-wave solution, as detailed in Section II-D.
3) Then, based on (9), we construct the phase-informed basis functions and compute the wave field $u(\mathbf{x})$ in the high-frequency region, as detailed in Section II-E.
4) We compare the phase difference between two solutions and repeat steps 2) and 3) until convergence. Finally, we perform postprocessing to obtain the field distribution and radar cross section (RCS).

C. Full-Wave HDG Method in the Low-Frequency Region

In order to obtain the wave propagation directions $\mu_n(\mathbf{x})$ in (9), we first use the full-wave HDG method to compute the wave field $u(\mathbf{x})$ in the relatively low-frequency region. Note that the full-wave solution involves abundant phase information for the computational domain with complex objects.

Within a finite region Ω and its boundary $\partial\Omega$, the Helmholtz equation reads

$$\begin{aligned} -\Delta u - k_{\mathrm{lf}}^2 u &= f, \quad \text{in } \Omega \\ \boldsymbol{n}^\top \nabla u + i\beta k_{\mathrm{lf}} u &= g, \quad \text{on } \partial\Omega \end{aligned} \tag{11}$$

where k_{lf} is the inhomogeneous wavenumber in the relatively low-frequency region, f denotes the source, and $\boldsymbol{n}$ is the outward normal vector. Note that the second equation is the Sommerfeld radiation condition. β and g are the boundary data determining the boundary types. Specifically, the Dirichlet boundary Γ_D corresponds to $\beta = \infty$, the Neumann boundary Γ_N corresponds to $\beta = 0$, and the first-order absorbing boundary Γ_R to $\beta = 1$ and $g = 0$. In addition, it is worth mentioning that the boundary in (11) can be readily replaced with perfectly matched layers (PMLs) [36].

Note that (11) represents a second-order partial differential equation (PDE) concerning the variable u. Subsequently, we introduce an intermediate variable $\boldsymbol{q}$, yielding two first-order PDEs

$$\begin{aligned} \boldsymbol{q} - \nabla u &= 0, \quad \text{in } \Omega \\ -\nabla \cdot \boldsymbol{q} - k_{\mathrm{lf}}^2 u &= f, \quad \text{in } \Omega \\ \boldsymbol{n}^\top \boldsymbol{q} + i\beta k_{\mathrm{lf}} u &= g, \quad \text{on } \partial\Omega. \end{aligned} \tag{12}$$

Now, consider partitioning Ω into $\mathrm{n_e}$ disjoint subdomains as follows:

$$\Omega = \bigcup_{h=1}^{\mathrm{n_e}} \Omega_h \tag{13}$$

with the union of inner interfaces Γ_I defined as follows:

$$\Gamma_I = \bigcup_{h=1}^{\mathrm{n_e}} \partial\Omega_h \backslash \partial\Omega \tag{14}$$

where $\partial\Omega_h$ denotes the boundary of Ω_h.

Subsequently, we establish governing equations at an element level as follows:

$$\begin{aligned} \boldsymbol{q}_h - \nabla u_h &= 0, \quad \text{in } \Omega_h \\ -\nabla \cdot \boldsymbol{q}_h - k_{\mathrm{lf}}^2 u_h &= f_h, \quad \text{in } \Omega_h \end{aligned} \tag{15}$$

with boundary conditions on $\partial\Omega_h$ at the element level as follows:

$$\begin{aligned} u_h &:= \widehat{u}_h \\ \boldsymbol{q}_h &:= \widehat{\boldsymbol{q}}_h. \end{aligned} \tag{16}$$

It is worth noting that two new variables $\widehat{u}_h$ and $\widehat{\boldsymbol{q}}_h$ are introduced, acting as new boundary conditions on $\partial\Omega_h$.

Note that u_h and $\boldsymbol{q}_h$ can be obtained locally through (15) and (16), referred to as the local problem. This aligns closely with the classical DG method.

However, the HDG discretization is not yet finalized, since (16) solely addresses the problem at an element level, lacking global connectivity across different elements.

Therefore, it is imperative to establish global connections across adjacent elements on the mesh skeleton Γ. Specifically, the inner continuity conditions and the outer boundary condition for variable $\widehat{u}$ and $\widehat{\boldsymbol{q}}$ on the mesh skeleton Γ are defined as follows:

$$\begin{aligned} [\![\boldsymbol{n}^\top \widehat{u}]\!]_\gamma &= \boldsymbol{0}, \quad \text{on} \quad \forall \gamma \in \Gamma_I \\ [\![\boldsymbol{n}^\top \widehat{\boldsymbol{q}}]\!]_\gamma &= 0, \quad \text{on} \quad \forall \gamma \in \Gamma_I \\ \boldsymbol{n}^\top \widehat{\boldsymbol{q}} + i\beta k_{\mathrm{lf}} \widehat{u} &= g, \quad \text{on} \quad \partial\Omega \end{aligned} \tag{17}$$

where

$$[\![\boldsymbol{n}^\top \vartheta]\!]_\gamma = \boldsymbol{n}_i^\top \vartheta_i + \boldsymbol{n}_j^\top \vartheta_j \tag{18}$$

is a jump operator across an inner interface γ shared by two neighboring elements Ω_i and Ω_j; $\boldsymbol{n}_i^\top$ denotes the outer normal vector for $\partial\Omega_i$; and ϑ_i refers to a variable, either scalar or vector, in the element Ω_i.

It should be emphasized that the HDG method transfers elemental boundary conditions (16) into global governing equations (17) on the mesh skeleton Γ. This is the unique property that the classical DG method does not have, referred to as the global problem.

The numerical flux connecting two interface variables $\widehat{\boldsymbol{q}}_h$ and $\widehat{u}_h$ is expressed as follows:

$$\boldsymbol{n}^\top \widehat{\boldsymbol{q}}_h - \boldsymbol{n}^\top \boldsymbol{q}_h = \tau(\widehat{u}_h - u_h) \tag{19}$$

where τ denotes a stabilization parameter, notably influencing the accuracy, stability, and convergence of the results [16], [37], [38]. Here, we choose the stabilization parameter as follows [27]:

$$\tau = ik_{\mathrm{lf}}. \tag{20}$$

Afterward, the HDG method employs polynomial approximation spaces $\boldsymbol{V}_h$, W_h, and $\widehat{M}_h$ for the classical basis functions as follows:

$$\begin{aligned} \boldsymbol{V}_h &:= \boldsymbol{t}(\mathbf{x}) \\ W_h &:= w(\mathbf{x}) \\ \widehat{M}_h &:= \mu(\mathbf{x}). \end{aligned} \tag{21}$$

In a single element Ω_h, for $h = 1, \ldots, \mathrm{n_e}$, we construct the local problem in the HDG method by testing (15) with $\forall\, \boldsymbol{t} \in \boldsymbol{V}_h$ and $\forall w \in W_h$, and computing integral by parts with the Gaussian divergence theorem as follows:

$$\begin{aligned} \left(\boldsymbol{t}, \boldsymbol{q}_h\right)_{\Omega_h} + \left(\nabla \cdot \boldsymbol{t}, u_h\right)_{\Omega_h} - \left\langle \boldsymbol{n}^\top \boldsymbol{t}, \widehat{u}_h \right\rangle_{\partial\Omega_h} &= 0 \\ -\left\langle w, \boldsymbol{n}^\top \widehat{\boldsymbol{q}}_h \right\rangle_{\partial\Omega_h} + \left(\nabla w, \boldsymbol{q}_h\right)_{\Omega_h} - \left(w, k_{\mathrm{lf}}^2 u_h\right)_{\Omega_h} &= \left(w, f_h\right)_{\Omega_h}. \end{aligned} \tag{22}$$

Note that by employing the numerical flux (19), we can eliminate $\widehat{\boldsymbol{q}}_h$. Consequently, two local dependent variables, u_h and q_h, can be solved at the element level, provided that $\widehat{u}_h$ is known.

On the mesh skeleton Γ, we construct the global problem in the HDG method by testing (17) with $\forall \mu \in \widehat{M}_h$, and computing surface integrals on the mesh skeleton Γ as follows:

$$\begin{aligned} &\sum_{h=1}^{\mathrm{n_e}} \left\{ \left\langle \mu, \boldsymbol{n}^\top \boldsymbol{q}_h \right\rangle_{\partial\Omega_h} + \left\langle \mu, \tau(\widehat{u}_h - u_h) \right\rangle_{\partial\Omega_h} + \left\langle \mu, i\beta k_{\mathrm{lf}} \widehat{u}_h \right\rangle_{\partial\Omega_h} \right\} \\ &= \sum_{h=1}^{\mathrm{n_e}} \left\{ \langle \mu, g \rangle_{\partial\Omega} \right\} \end{aligned} \tag{23}$$

where the global problem has been divided into an accumulation of surface integrals in $\mathrm{n_e}$ local elements. Note that two local dependent variables u_h and $\boldsymbol{q}_h$ in (23) can be eliminated through the local equation (22).

We should note that the HDG method shows superior stability, convergence, and efficiency compared with the traditional numerical methods, such as the finite-difference method and the finite-element method [27], [39].

D. Phase Extraction Technique

Subsequently, we introduce a phase extraction technique to determine the wave propagation directions, denoted as $\mu_n(\mathbf{x})$ in (9), from the full-wave solution in the low-frequency region. We would like to introduce the NMLA method, since it offers a simpler and more robust approach [40].

The fundamental assumption in the NMLA method is that a wave field $u(\mathbf{x})$ can be locally approximated as a superposition of plane waves with different propagation directions. Specifically, on a small neighborhood around an observation point $\mathbf{x}_0$, we have

$$u(\mathbf{x}) = \sum_{m=1}^{L} B_m e^{ik(\mathbf{x}-\mathbf{x}_0)\cdot\widehat{\mathbf{d}}_m}, \quad \left|\widehat{\mathbf{d}}_m\right| = 1 \tag{24}$$

where L is the number of plane waves, B_m is the magnitude, and $\widehat{\mathbf{d}}_m = (\cos\xi_m, \sin\xi_m)$ is the wave propagation direction corresponding to the mth plane wave. ξ_m is the corresponding angle.

In particular, consider a circle with the radius r centered at $\mathbf{x}_0$, and introduce the angle notation θ; the point on the circle can be expressed through the polar coordinates as follows:

$$\mathbf{x}(\theta) = \mathbf{x}_0 + r\widehat{\mathbf{s}}(\theta) \tag{25}$$

where $\widehat{\mathbf{s}}(\theta) = (\cos\theta, \sin\theta)$. The wave field $u(\mathbf{x}(\theta))$ on the circle can be further stated as follows:

$$u(\mathbf{x}(\theta)) = \sum_{m=1}^{L} B_m e^{ikr\widehat{\mathbf{s}}\cdot\widehat{\mathbf{d}}_m}. \tag{26}$$

Subsequently, we sample the impedance quantity $I(\theta)$ on the circle as follows:

$$I(\theta) := \frac{1}{ik}\partial_r u(\mathbf{x}(\theta)) + u(\mathbf{x}(\theta)) \tag{27}$$

where $\partial_r u(\mathbf{x}(\theta))$ is the derivative of the wave field $u(\mathbf{x}(\theta))$. Note that $I(\theta)$ effectively eliminates any potential ambiguity due to resonance and enhances the robustness of solutions in the presence of noise [40].

Actually, in our numerical framework, the wave field $u(\mathbf{x}(\theta))$ and its derivative $\partial_r u(\mathbf{x}(\theta))$ have been computed in Section II-C. Therefore, the sampling procedure (27) is a postprocessing procedure, and the computational cost can be considered negligible.

We further apply the filtering operator $\mathcal{B}$ to process the impedance quantity $I(\theta)$, which can be expressed as follows:

$$\mathcal{B}I(\theta) = \sum_{m=1}^{L} B_m S_l(\theta - \xi_m) \tag{28}$$

with

$$S_l(\theta) = \frac{\sin([2l+1]\theta/2)}{[2l+1]\sin(\theta/2)}. \tag{29}$$

Finally, at an observation point $\mathbf{x}_0$, we can determine the wave propagation directions $\mu_n(\mathbf{x}_0)$ as follows:

$$\mu_n(\mathbf{x}_0) = \theta_n, \quad n = 1, 2, \ldots \tag{30}$$

where $\mathcal{B}I(\theta_n)$ is the local maximum in the filtered data (28). It should be emphasized that the NMLA method is essentially a signal-processing method, since it extracts the wave propagation directions $\mu_n(\mathbf{x}_0)$ at $\mathbf{x}_0$ by sampling and processing the wave field $u(\mathbf{x}(\theta))$. More details of the NMLA method can be referred to [40] and [41].

E. Phase-Informed HDG Method in the High-Frequency Region

Now, we step into the PI-HDG discretization. In a single element Ω_h, we have obtained the elemental phase information $\varphi_h(\mathbf{x})$ from Section II-D, which is the set of $\mu_n(\mathbf{x}_0)$ within the element. Then, the local approximation spaces $\boldsymbol{V}_h^*$, W_h^*, and $\widehat{M}_h^*$ for the phase-informed basis functions are defined as follows:

$$\begin{aligned} \boldsymbol{V}_h^* &:= \boldsymbol{t}(\mathbf{x})\exp(ik_{\mathrm{hf}}\varphi_h(\mathbf{x})) \\ W_h^* &:= w(\mathbf{x})\exp(ik_{\mathrm{hf}}\varphi_h(\mathbf{x})) \\ \widehat{M}_h^* &:= \mu(\mathbf{x})\exp(ik_{\mathrm{hf}}\varphi_h(\mathbf{x})) \end{aligned} \tag{31}$$

where the amplitude values $\boldsymbol{t}(\mathbf{x})$, $w(\mathbf{x})$, and $\mu(\mathbf{x})$ are derived from finite-dimensional polynomial spaces $\boldsymbol{V}_h$, W_h, and $\widehat{M}_h$ in (21), respectively, and k_{hf} is the wavenumber in the high-frequency region.

It is remarkable that these novel local approximation spaces defined in (31) incorporate prior physical information from the low-frequency solution. This allows us to focus primarily on the computation of amplitudes.

Now, we are ready to describe our PI-HDG numerical scheme of the Helmholtz equation through the proposed phase-informed basis functions. We find $(\boldsymbol{q}_h, u_h, \widehat{u}_h) \in \boldsymbol{V}_h^* \times W_h^* \times \widehat{M}_h^*$, such that the following equations:

$$\begin{aligned} &\left(\boldsymbol{t}^*, \boldsymbol{q}_h\right)_{\Omega_h} + \left(\nabla\cdot\boldsymbol{t}^*, u_h\right)_{\Omega_h} - \left\langle \boldsymbol{n}^\top\boldsymbol{t}^*, \widehat{u}_h\right\rangle_{\partial\Omega_h} \\ &\quad = 0 - \left\langle w^*, \boldsymbol{n}^\top\widehat{\boldsymbol{q}}_h\right\rangle_{\partial\Omega_h} + \left(\nabla w^*, \boldsymbol{q}_h\right)_{\Omega_h} - (w^*, k_{\mathrm{hf}}^2 u_h)_{\Omega_h} \\ &\quad = (w^*, f_h)_{\Omega_h} \end{aligned} \tag{32}$$

with boundary condition

$$\begin{aligned} &\sum_{h=1}^{\mathrm{n_e}}\left\{\left\langle\mu^*, \boldsymbol{n}^\top\boldsymbol{q}_h\right\rangle_{\partial\Omega_h} + \left\langle\mu^*, \tau(\widehat{u}_h - u_h)\right\rangle_{\partial\Omega_h} + \left\langle\mu^*, i\beta k_{\mathrm{hf}}\widehat{u}_h\right\rangle_{\partial\Omega_h}\right\} \\ &\quad = \sum_{h=1}^{\mathrm{n_e}}\left\{\left\langle\mu^*, g\right\rangle_{\partial\Omega}\right\} \end{aligned} \tag{33}$$

hold for all $(\boldsymbol{t}^*, w^*, \mu^*) \in \boldsymbol{V}_h^* \times W_h^* \times \widehat{M}_h^*$.

The weak formulation of the PI-HDG method, as expressed in (32) and (33), closely resembles that of the full-wave HDG method, outlined in (22) and (23). The primary distinction lies in the approximation spaces. This dissimilarity renders the PI-HDG method notably superior in both accuracy and efficiency compared with the classical full-wave method in the high-frequency modeling [27].

III. Numerical Experiments

A. Analytical Solution for the Helmholtz Equation

We begin with an analytical example in order to illustrate the accuracy, convergence, and especially extensibility of the proposed method. We consider the Helmholtz equation (11) in a square $\Omega = [-1, 1] \times [-1, 1] \subset \mathbb{R}^2$ with a Robin boundary condition as follows:

$$\nabla u \cdot \boldsymbol{n} + iku = g_{\mathrm{R}}, \quad \text{on } \partial\Omega. \tag{34}$$

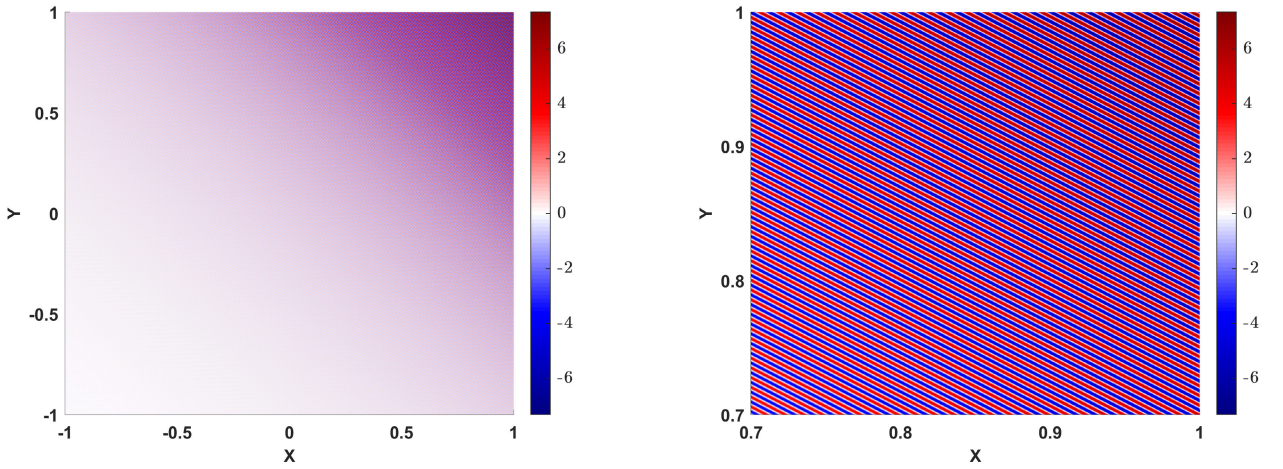

(a) (b)

Fig. 2. (a) Result of u in $k = 1000$ ($\lambda = 6.28 \times 10^{-3}$) by the PI-HDG method, where the mesh size $h = 1/16$ and the polynomial degree p is 1; the L^2-norm error is 1.92×10^{-3}. (b) Local magnification at $[0.7, 1] \times [0.7, 1]$, with more than 47 wavelengths in the region (units have been normalized).

Here, we choose the source term f and boundary data g_R, such that the problem has the following exact solution:

$$u_{ex} = A(x, y)\exp(ik\varphi(x, y)) \tag{35}$$

with $A(x, y) = \exp(x + y)$ and $\varphi(x, y) = (1/2)x + (\sqrt{3}/2)y$. Note that (35) is identical in form to asymptotic expansion (6), making it highly suitable for testing the fundamental properties. We consider polynomial degrees $p = 1 - 4$ using nodal basis functions within each element, for space discretization. The L^2-norm error is defined as follows:

$$u_{err} = \frac{\|u - u_{ref}\|_2}{\|u_{ref}\|_2} \tag{36}$$

where u and u_{ref} are the column vectors composed of the numerical result and analytical (reference) result, respectively.

1) Convergence Test: We first test the convergence of the PI-HDG method. We consider triangular meshes with mesh sizes of $h = 1/2^n (n = 1, 2, 3, 4)$ and the wavenumber $k = 1000$ (the wavelength $\lambda = 6.28 \times 10^{-3}$). Fig. 2(a) gives the result of u where the mesh size $h = 1/16$ and the polynomial degree p is 1; the L^2-norm error is 1.92×10^{-3}. Fig. 2(b) provides local magnification at $[0.7, 1] \times [0.7, 1]$, with more than 47 wavelengths in the region. Fig. 3 shows the convergence of the L^2-norm error u_{err}, as a function of the characteristic mesh size h, for polynomial degrees $p = 1 - 4$. Fig. 3 shows that the PI-HDG method maintains the optimal convergence of order $p+1$ as the classical HDG scheme [18].

2) Extensibility Test: On the same mesh size, we further test the growth rate of the L^2-norm error as k increases. We use 512 triangular elements in the computational domain with polynomial degrees $p =$ 1–4. We consider the wavenumber k from 10^0 to 10^4 (the wavelength λ from 6.28 to 6.28×10^{-4}). Fig. 4 shows the relationship between the L^2-norm error u_{err} and the wavenumber k. Because of phase-informed basis functions, the L^2-norm error remains almost unchanged. It also validates that the proposed method alleviates the problem of highly exponential oscillatory integral computation. Of course, this is the most ideal scenario, as the phase information is known, and the asymptotic expansion (6) agrees with the exact solution.

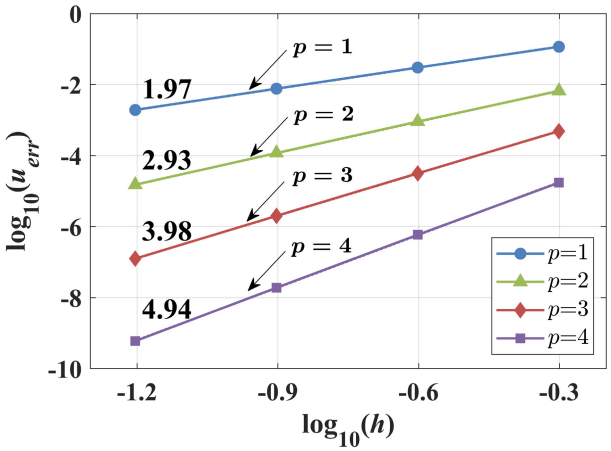

Fig. 3. Convergence of the L^2-norm error u_{err}, as a function of the characteristic mesh size h, for polynomial degrees $p = 1 - 4$, where the wavenumber $k = 1000$ (the wavelength $\lambda = 6.28 \times 10^{-3}$).

B. Plane Wave Scattering From a Square Target With One Jagged Edge

This example aims to consider scenarios involving multiple reflections. We consider the exterior Helmholtz problem for scattering of an incident plane wave $u^{\text{inc}} = \exp(ikx)$ by a square target with one jagged edge. Note that we adopt the scattering field as the unknown variable; thus, the Dirichlet boundary condition is expressed as $u = -u^{\text{inc}}$ on each edge of the square target and the Robin boundary condition as $\nabla u \cdot \boldsymbol{n} + iku = g$ on the boundary of the computational domain. Here, the boundary data are obtained as $g = 0$, representing the first-order absorbing condition.

Fig. 5 presents the ray trajectories obtained by the COMSOL software with the ray optics module [42], and the color of rays represents the optical path length. It can be observed that

TABLE I
CALCULATION SCALE AND RESOURCE CONSUMPTION BETWEEN TWO METHODS IN $k = 100$

	Element number	Basis order	PPW	Global DoFs	Solving time	Memory peak	Error
FEM	1 917 537	2nd	20.94	3 839 247	483 s	32.9 GB	3.03 %
PI-HDG	39 659	2nd	3.14	237 954	45 s	2.0 GB	2.78 %

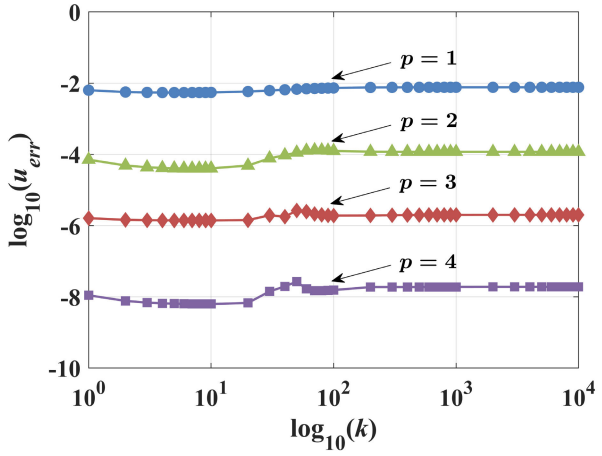

Fig. 4. L^2-norm error of the PI-HDG method remains almost unchanged as k increases from 10^0 to 10^4 (λ from 6.28 to 6.28 $\times$ 10^{-4}).

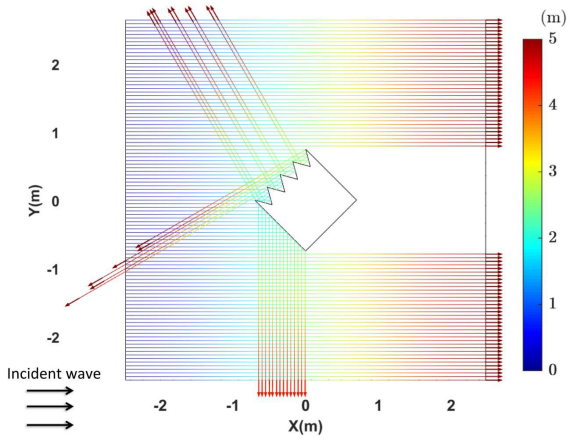

Fig. 5. Ray trajectories and optical path length obtained by the COMSOL software with the ray optics module [42]. Only the reflected rays are calculated, lacking sufficient phase information.

only the reflected rays are calculated. Obviously, this phase information is insufficient. While some literature, such as [43], proposes analytical methods for diffraction rays computation, there have been persistent issues regarding universality. Therefore, we prefer to extract the wave propagation directions based on the full-wave solution in the low-frequency region, since it involves abundant phase information.

In the low-frequency full-wave computation, we consider triangular meshes with the mesh size $h = 0.04$ m, the polynomial degree $p = 2$, and the wavenumber $k = 10$ (the wavelength $\lambda = 0.628$ m). The PPW is defined as follows:

$$\text{PPW} = \frac{\lambda p}{h} = \frac{2\pi p}{kh}. \tag{37}$$

Therefore, the PPW in the low-frequency region is 31.42. Here, the PPW is slightly higher than the rule of thumb, allowing us to obtain a more accurate solution in the low-frequency region. Fig. 6(a) shows the result of the scattering field by the PI-HDG method in the low-frequency region where $k = 10$ ($\lambda = 0.628$ m). We also compare our result with the commercial software COMSOL, which uses the full-wave FEM method. The mesh size $h = 0.005$ m, the polynomial degree $p = 4$, and the PPW is 502.65. Fig. 6(b) gives the full-wave reference result. Fig. 6(c) gives the absolute error (with ten times magnification) of the scattering field between two methods, and the L^2-norm error is 1.05×10^{-3}.

Afterward, on the low-frequency mesh, we evaluate the performance in the high-frequency region. Fig. 7(a) gives the result of the scattering field by the PI-HDG method in the high-frequency region where $k = 100$ ($\lambda = 0.0628$ m). Fig. 7(b) gives the full-wave reference result. Fig. 7(c) gives the absolute error of the scattering field between two methods, and the L^2-norm error is 2.78×10^{-2}. Since we adopt the same mesh size $h = 0.04$ m and polynomial degree $p = 2$ as in the low-frequency region, the PPW here is 3.14, remarkably less than the rule of thumb. Table I gives the calculation scale and resource consumption between two methods under a similar error level in $k = 100$. It highlights that compared with the full-wave FEM software, the temporal consumption of the PI-HDG method is only 1/10, while the memory is 1/16. In particular, the computation in the low-frequency region takes 19.5 s, the phase extraction step takes 3.4 s, and the computation in the high-frequency region takes 22.2 s, while we ignore the I/O cost. We emphasize that by employing appropriate parallel schemes, the cost of phase extraction can be further reduced. Therefore, the cost incurred in the numerical framework is approximately two times the computation cost in the low-frequency region.

Fig. 8 shows the bistatic RCS calculated by the PI-HDG method and the COMSOL software in the low- and high-frequency regions, respectively. The root-mean-square error (RMSE) is defined as follows:

$$\text{RMSE(dB)} = \sqrt{\frac{1}{N}\sum |\sigma - \sigma_{ref}|^2} \tag{38}$$

where N is the number of sample points, and σ and σ_{ref} are the RCS results by the PI-HDG and full-wave FEM method, respectively. The RMSE between two methods in the log scale in the low-frequency region is 0.02 dB, while the high-frequency region is 1.45 dB.

C. Plane Wave Scattering From a Dielectric Circle

This example aims to consider scenarios involving an inhomogeneous object. We consider the exterior Helmholtz

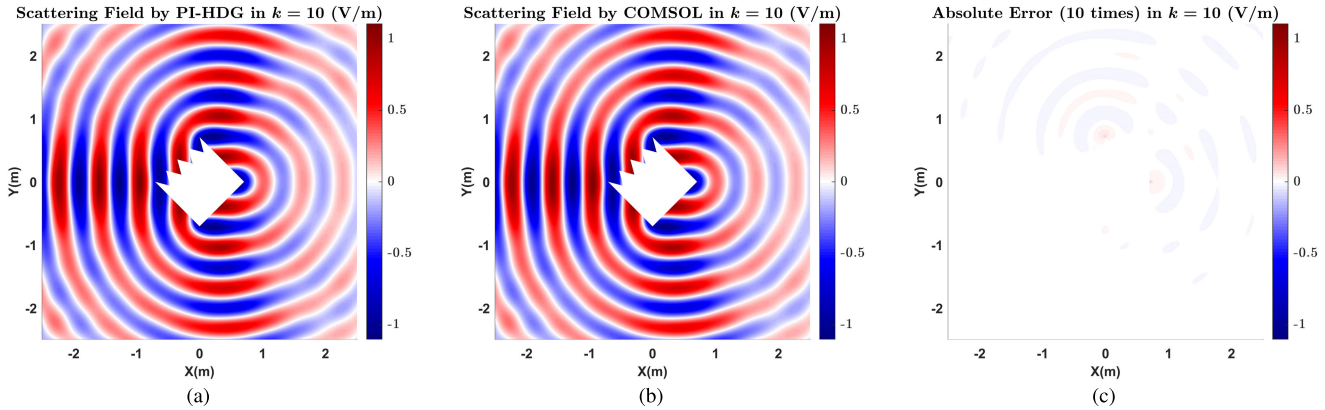

Fig. 6. Result of the scattering field by (a) PI-HDG method and (b) full-waveform COMSOL software in the low-frequency region where $k = 10$, with more than seven wavelengths in the region. (c) Absolute error (with ten times magnification) between (a) and (b), and the L^2-norm error is 1.06×10^{-3}.

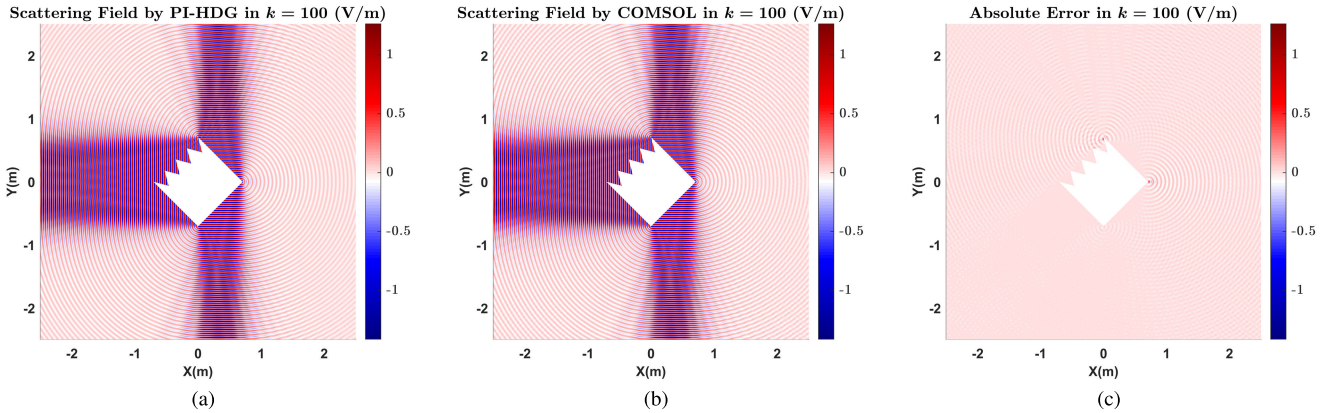

Fig. 7. Result of the scattering field by (a) PI-HDG method and (b) full-waveform COMSOL software in the high-frequency region where $k = 100$, with more than 79 wavelengths in the region. (c) Absolute error of the scattering field between (a) and (b), and the L^2-norm error is 2.78×10^{-2}.

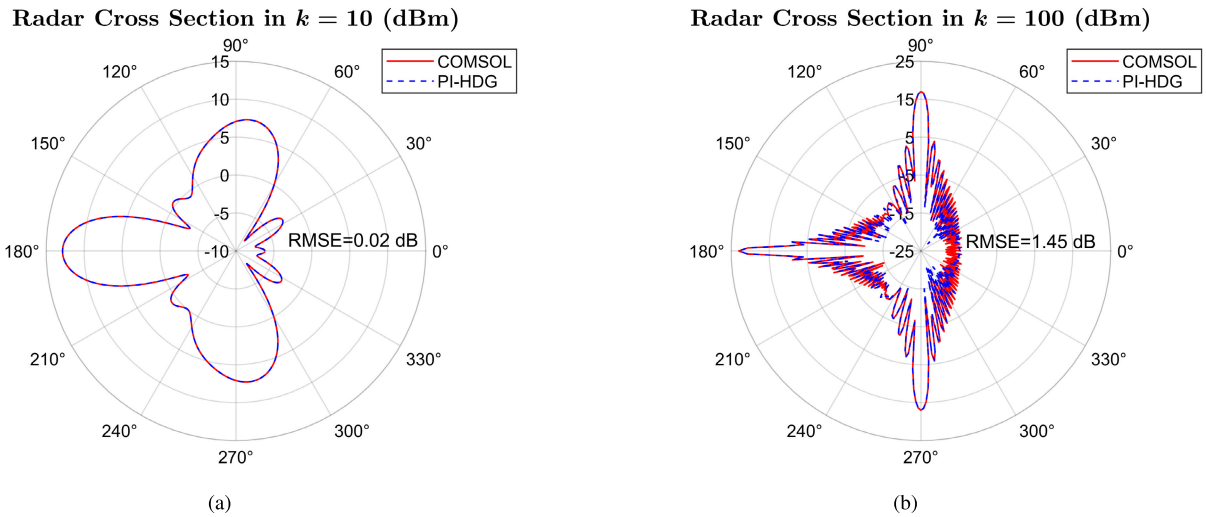

Fig. 8. Bistatic RCS by the PI-HDG method and the full-waveform COMSOL software in (a) low-frequency region where $k = 10$ (Fig. 6) and (b) high-frequency region where $k = 100$ (Fig. 7).

problem for scattering of an incident plane wave $u^{\text{inc}} = \exp(ikx)$ by a dielectric circle with a radius of 0.5 m. The relative permittivity increases linearly from 1 to 9 as the radius decreases from 0.5 to 0 m. Since there is no Dirichlet boundary inside, we use the total field as the unknown variable; thus, the Robin boundary condition is $\nabla u \cdot \boldsymbol{n} + iku = 0$ on the boundary of the computational domain.

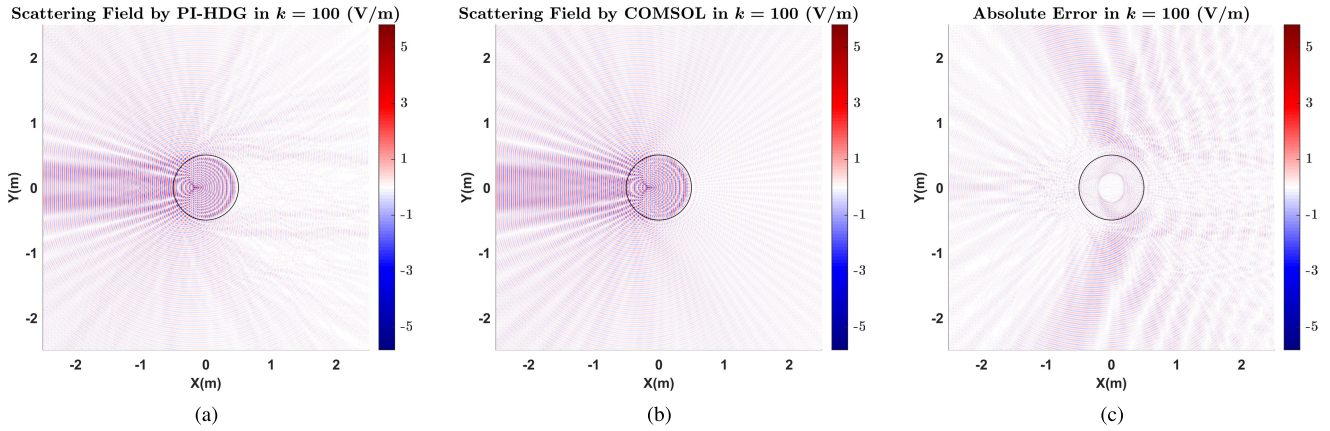

Fig. 9. Result of the scattering field by (a) PI-HDG method and (b) full-waveform COMSOL software in the high-frequency region where $k = 100$, with more than 79 wavelengths in the region. (c) Absolute error of the scattering field between (a) and (b).

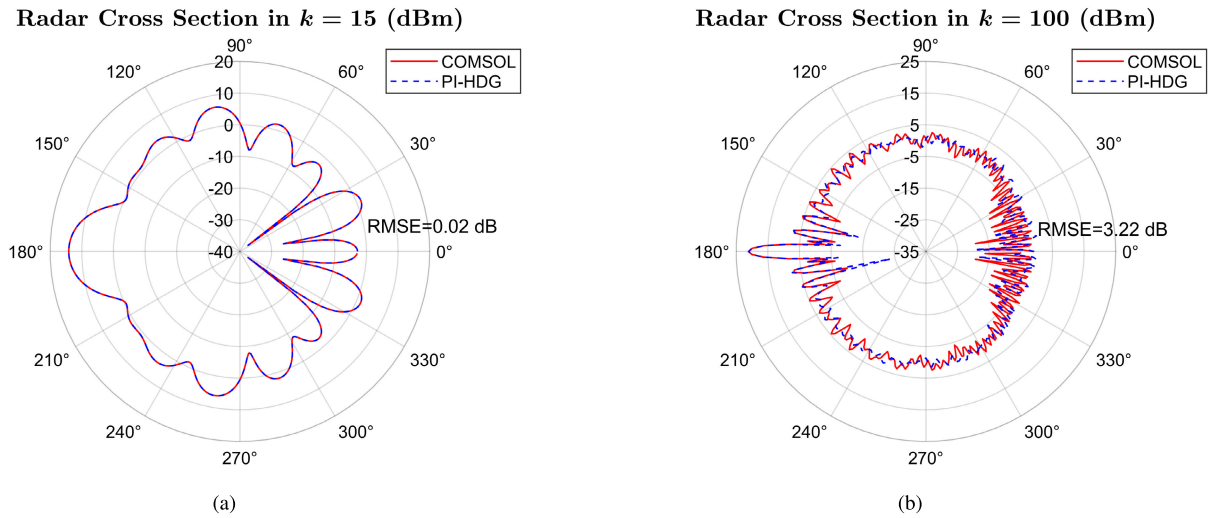

Fig. 10. Bistatic RCS by the PI-HDG method and the full-waveform COMSOL software in (a) low-frequency region where $k = 15$ and (b) high-frequency region where $k = 100$ (Fig. 9).

We consider triangular meshes with the mesh size $h = 0.04$ m and the polynomial degree $p = 3$. The wavenumber in the low-frequency region is $k = 15$ (the wavelength $\lambda = 0.4188$ m).

Fig. 9(a) gives the result of the scattering field by the PI-HDG method in the high-frequency region where $k = 100$ ($\lambda = 0.0628$ m). Fig. 9(b) gives the full-wave reference result, where the mesh size $h = 0.005$ m and the polynomial degree $p = 5$. Fig. 9(c) gives the absolute error of the scattering field between two methods. The PPW here is 4.71, less than the rule of thumb. Fig. 10 shows the bistatic RCS calculated by the PI-HDG method and the COMSOL software in the low- and high-frequency regions, respectively. The RMSE between two methods in the log scale in the low-frequency region is 0.02 dB, while the high-frequency region is 3.22 dB. Despite the relatively large absolute error, the RCS agrees well, because it requires less field information. We will adopt the scattering field as the unknown variable to enhance phase extraction accuracy in future work.

D. Plane Wave Scattering From an Airplane

Sections III-A–III-C demonstrate the convergence, accuracy, and efficiency of the proposed algorithm. This example further considers a more realistic scenario. We consider the exterior Helmholtz problem for scattering of an incident plane wave $u^{\text{inc}} = \exp(ikx)$ by an airplane. The computation area is 50×50 m^2. Note that we adopt the scattering field as the unknown variable; thus, the Dirichlet boundary condition is expressed as $u = -u^{\text{inc}}$ on the surface of the airplane, and the Robin boundary condition is $\nabla u \cdot \boldsymbol{n} + iku = g$ on the boundary of the computational domain. Here, the boundary data are obtained as $g = 0$, representing the first-order absorbing condition.

In the low-frequency full-wave computation, we consider triangular meshes with the mesh size $h = 0.06$ m, the wavenumber $k = 4\pi$, the polynomial degree $p = 3$, and the PPW is 25. The computational domain contains 100 wavelengths, since the wavelength $\lambda = 0.5$ m.

Fig. 11(a) gives the result of the scattering field by the PI-HDG method in the low-frequency region where $k = 4\pi$.

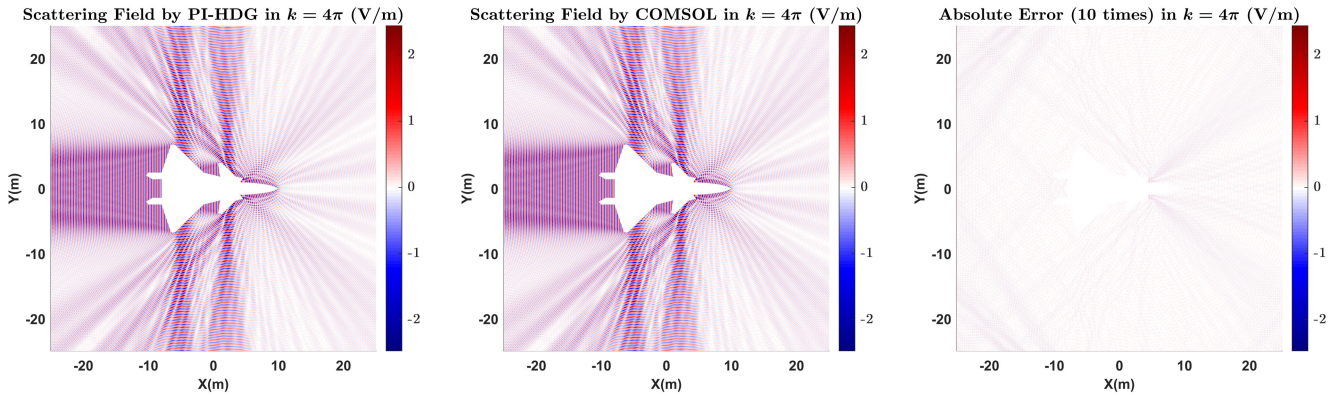

Fig. 11. (a) Result of the scattering field by (a) PI-HDG method and (b) full-waveform COMSOL software in the low-frequency region where $k = 4\pi$, with 100 wavelengths in the region. (c) Absolute error (with ten times magnification) of the scattering field between (a) and (b), and the L^2-norm error is 8.72×10^{-3}.

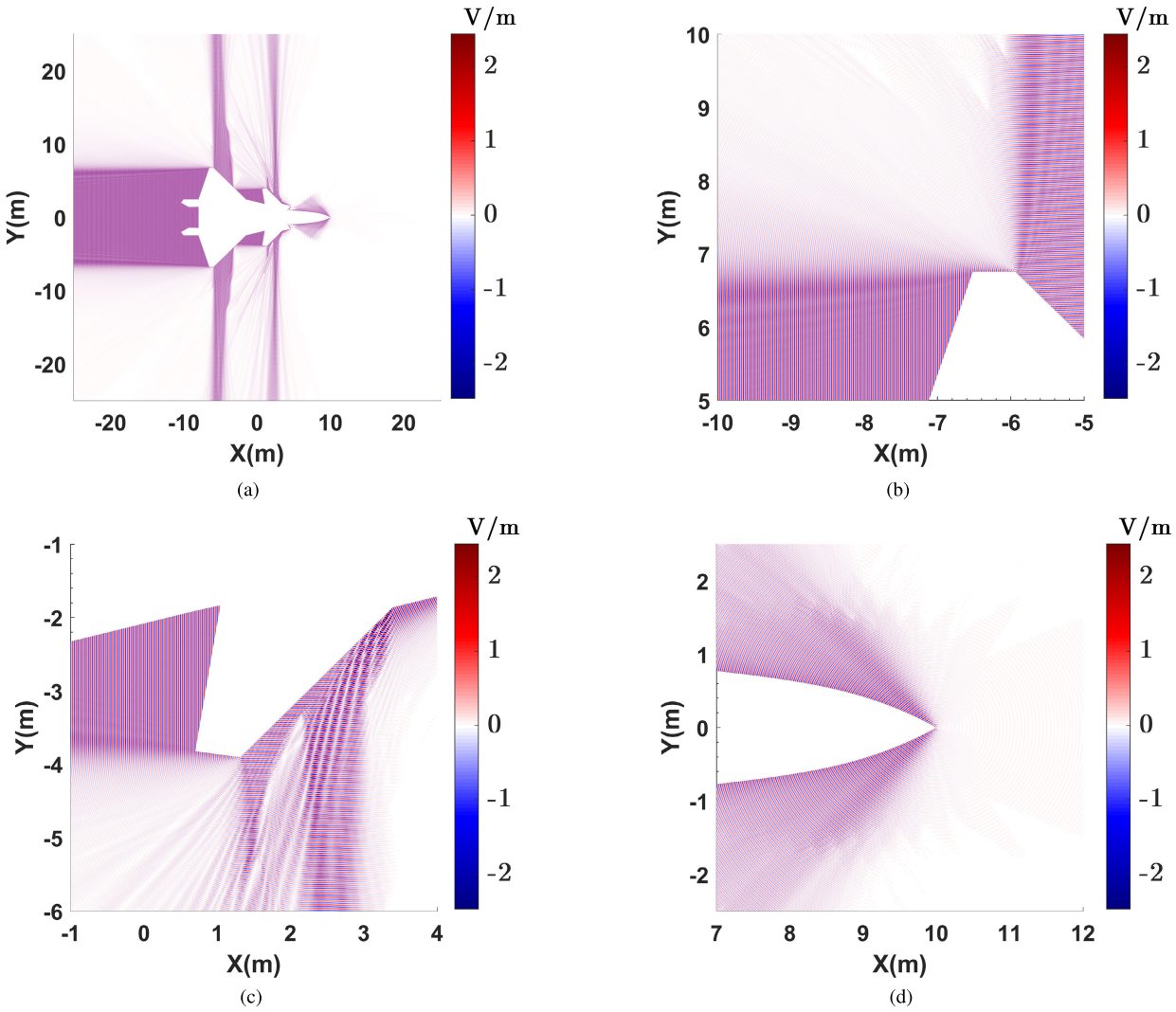

Fig. 12. (a) Scattering field distribution by the PI-HDG method in $k = 40\pi$, with 1000 wavelengths in the region. The mesh size is 0.06 m, the polynomial degree is 3, and the PPW is 2.5. (b)–(d) Local magnification at $[-10, -5] \times [5, 10]$ m^2, $[-1, 4] \times [-6, -1]$ m^2, and $[7, 12] \times [-2.5, 2.5]$ m^2, respectively.

We also compare our result with the commercial software COMSOL. The mesh size $h = 0.04$ m and the polynomial degree $p = 5$, and the PPW is 62.5. Fig. 11(b) gives the full-wave reference result. Fig. 11(c) gives the absolute error (with ten times magnification) of the scattering field between two methods, and the L^2-norm error is 8.72×10^{-3}.

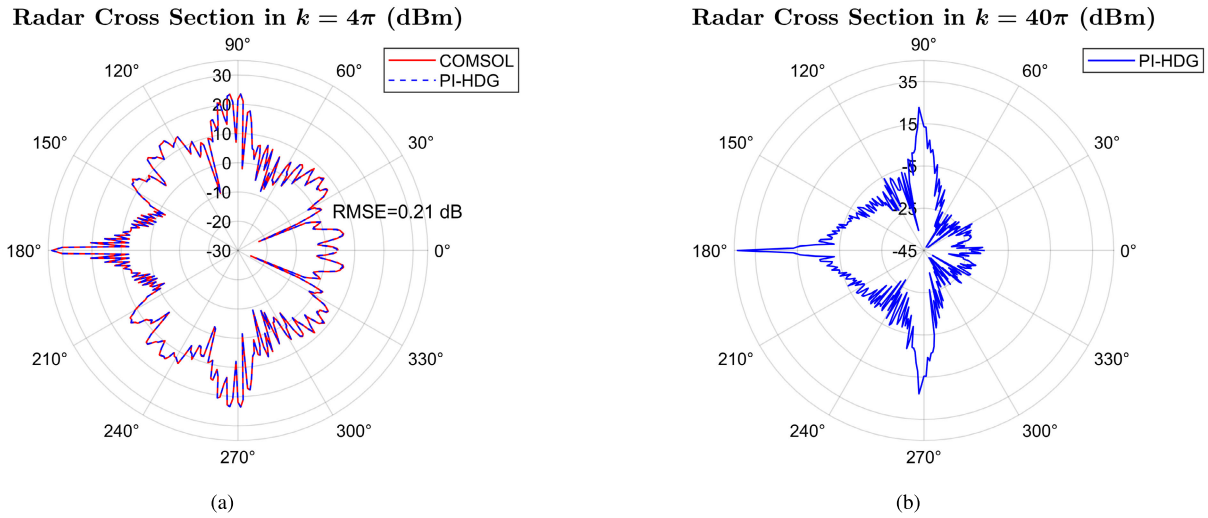

Fig. 13. Bistatic RCS in (a) low-frequency region where $k = 4\pi$ (Fig. 11) and (b) high-frequency region where $k = 40\pi$ (Fig. 12).

We further validate the extensibility of the proposed algorithm. Fig. 12(a) gives the result of the scattering field by the PI-HDG method in the high-frequency region where $k = 40\pi$. Note that the computational domain contains 1000 wavelengths, since the wavelength $\lambda = 0.05$ m. Fig. 12(b)–(d) provides local magnification at $[-10, -5] \times [5, 10]$ m^2, $[-1, 4] \times [-6, -1]$ m^2, and $[7, 12] \times [-2.5, 2.5]$ m^2, respectively. Besides, Since we adopt the same mesh size $h = 0.06$ m and polynomial degree $p = 3$ as in the low-frequency region, the PPW here is 2.5, remarkably less than the rule of thumb.

Fig. 13(a) shows the bistatic RCS calculated by the PI-HDG method and the COMSOL software in the low-frequency region where $k = 4\pi$. The RMSE between two methods in the log scale is 0.21 dB. Fig. 13(b) gives the RCS calculated by the PI-HDG method in the high-frequency region where $k = 40\pi$.

Furthermore, upon comparing the field distributions in Figs. 11(a) and 12(a), as well as the magnitude of the RCS in Fig. 13(a) and (b), we observe that the low-frequency results exhibit wave-like propagation characteristics, while the high-frequency results exhibit ray-like behaviors. This is aligned with the theory of the geometric optics ansatz.

IV. Conclusion

In this article, a PI-HDG method is presented for extremely high-frequency wave modeling. We integrate the prior knowledge of phase information into the construction of basis functions, thereby leveraging the strengths of both the HDG method and geometric optics ansatz. We extract the phase information based on the full-wave solution in the relative low-frequency region, since it involves abundant phase information. Rigorous analytical solutions demonstrate that optimal orders of convergence are achieved in the proposed algorithm. Furthermore, we achieve high-frequency scattering analysis of complex targets on the low-frequency mesh. Numerical results show that the temporal consumption is only 1/10, while the memory is 1/16, when compared with the reference finite-element software.

References

[1] M. K. Leino, J. Ala-Laurinaho, A. Höök, B. Svensson, and V. Viikari, "Low-scattering chopped dipole for secondary surveillance radar," *IEEE Trans. Antennas Propag.*, vol. 70, no. 3, pp. 1694–1705, Mar. 2022.

[2] M. T. Bevacqua, R. Palmeri, T. Isernia, and L. Crocco, "A simple procedure to design virtual experiments for microwave inverse scattering," *IEEE Trans. Antennas Propag.*, vol. 69, no. 12, pp. 8652–8663, Dec. 2021.

[3] L. Azpilicueta et al., "Diffuse-scattering-informed geometric channel modeling for THz wireless communications systems," *IEEE Trans. Antennas Propag.*, vol. 71, no. 10, pp. 8226–8238, Oct. 2023.

[4] Q. H. Liu, "The PSTD algorithm: A time-domain method requiring only two cells per wavelength," *Microw. Opt. Technol. Lett.*, vol. 15, no. 3, pp. 158–165, Jun. 1997.

[5] F. Ihlenburg and I. Babuška, "Finite element solution of the Helmholtz equation with high wave number—Part I: The h-version of the FEM," *Comput. Math. Appl.*, vol. 30, no. 9, pp. 9–37, 1995.

[6] F. Ihlenburg and I. Babuska, "Finite element solution of the Helmholtz equation with high wave number—pART II: The h-p version of the FEM," *SIAM J. Numer. Anal.*, vol. 34, no. 1, pp. 315–358, 1997.

[7] T. Chaumont-Frelet and S. Nicaise, "Wavenumber explicit convergence analysis for finite element discretizations of general wave propagation problems," *IMA J. Numer. Anal.*, vol. 40, no. 2, pp. 1503–1543, Apr. 2020.

[8] I. Babuška, F. Ihlenburg, E. T. Paik, and S. A. Sauter, "A generalized finite element method for solving the Helmholtz equation in two dimensions with minimal pollution," *Comput. Methods Appl. Mech. Eng.*, vol. 128, nos. 3–4, pp. 325–359, Dec. 1995.

[9] H. Wu, "Pre-asymptotic error analysis of CIP-FEM and FEM for the Helmholtz equation with high wave number. Part I: Linear version," *IMA J. Numer. Anal.*, vol. 34, no. 3, pp. 1266–1288, Jul. 2014.

[10] C. C. Stolk, M. Ahmed, and S. K. Bhowmik, "A multigrid method for the Helmholtz equation with optimized coarse grid corrections," *SIAM J. Sci. Comput.*, vol. 36, no. 6, pp. A2819–A2841, Jan. 2014.

[11] Q. Zhan, M. Zhuang, Y. Mao, and Q. H. Liu, "Unified Riemann solution for multi-physics coupling: Anisotropic poroelastic/elastic/fluid interfaces," *J. Comput. Phys.*, vol. 402, Feb. 2020, Art. no. 108961.

[12] Q. Zhan, Q. Sun, Q. Ren, Y. Fang, H. Wang, and Q. H. Liu, "A discontinuous Galerkin method for simulating the effects of arbitrary discrete fractures on elastic wave propagation," *Geophys. J. Int.*, vol. 210, no. 2, pp. 1219–1230, Aug. 2017.

[13] Q. Zhan, Q. Ren, Q. Sun, H. Chen, and Q. H. Liu, "Isotropic Riemann solver for a nonconformal discontinuous Galerkin Pseudospectral time-domain algorithm," *IEEE Trans. Geosci. Remote Sens.*, vol. 55, no. 3, pp. 1254–1261, Mar. 2017.

[14] M. Liu, K. Sirenko, and H. Bagci, "An efficient discontinuous Galerkin finite element method for highly accurate solution of Maxwell equations," *IEEE Trans. Antennas Propag.*, vol. 60, no. 8, pp. 3992–3998, Aug. 2012.

[15] Q. Zhan, Y. Fang, M. Zhuang, M. Yuan, and Q. H. Liu, "Stabilized DG-PSTD method with nonconformal meshes for electromagnetic waves," *IEEE Trans. Antennas Propag.*, vol. 68, no. 6, pp. 4714–4726, Jun. 2020.

[16] Q. Zhan et al., "An adaptive high-order transient algorithm to solve large-scale anisotropic Maxwell's equations," *IEEE Trans. Antennas Propag.*, vol. 70, no. 3, pp. 2082–2092, Mar. 2022.

[17] B. Cockburn and J. Gopalakrishnan, "A characterization of hybridized mixed methods for second order elliptic problems," *SIAM J. Numer. Anal.*, vol. 42, no. 1, pp. 283–301, Jan. 2004.

[18] B. Cockburn, B. Dong, and J. Guzmán, "A superconvergent LDG-hybridizable Galerkin method for second-order elliptic problems," *Math. Comput.*, vol. 77, no. 264, pp. 1887–1916, May 2008.

[19] M. Taus, L. Demanet, L. Z. Núñez, and R. Hewett, "Pollution-free and fast hybridizable discontinuous Galerkin solvers for the high-frequency Helmholtz equation," in *Proc. SEG Tech. Program Expanded Abstr.*, Aug. 2017, pp. 4068–4073.

[20] Y. Huang, Z. Zhao, Z. Nie, and Q.-H. Liu, "Dynamic volume equivalent SBR method for electromagnetic scattering of targets moving on the sea," *IEEE Trans. Antennas Propag.*, vol. 71, no. 4, pp. 3509–3519, Apr. 2023.

[21] C. Dong, L. Guo, X. Meng, and H. Li, "An improved GO-PO/PTD hybrid method for EM scattering from electrically large complex targets," *IEEE Trans. Antennas Propag.*, vol. 70, no. 12, pp. 12130–12138, Dec. 2022.

[22] I. Babuška and J. M. Melenk, "The partition of unity method," *Int. J. Numer. Methods Eng.*, vol. 40, no. 4, pp. 727–758, 1997.

[23] I. Perugia, P. Pietra, and A. Russo, "A plane wave virtual element method for the Helmholtz problem," *ESAIM: Math. Model. Numer. Anal.*, vol. 50, no. 3, pp. 783–808, May 2016.

[24] A. Buffa and P. Monk, "Error estimates for the ultra weak variational formulation of the Helmholtz equation," *ESAIM, Math. Model. Numer. Anal.*, vol. 42, no. 6, pp. 925–940, Nov. 2008.

[25] R. Hiptmair, A. Moiola, and I. Perugia, "A survey of Trefftz methods for the Helmholtz equation," in *Building Bridges: Connections and Challenges in Modern Approaches to Numerical Partial Differential Equations*. Cham, Switzerland: Springer, 2016, pp. 237–279.

[26] X. Li et al., "Scientific machine learning enables multiphysics digital twins of large-scale electronic chips," *IEEE Trans. Microw. Theory Techn.*, vol. 70, no. 12, pp. 5305–5318, Dec. 2022.

[27] N. C. Nguyen, J. Peraire, F. Reitich, and B. Cockburn, "A phase-based hybridizable discontinuous Galerkin method for the numerical solution of the Helmholtz equation," *J. Comput. Phys.*, vol. 290, pp. 318–335, Jun. 2015.

[28] Z. Nie, S. Ren, S. Yan, S. He, and J. Hu, "Modified phase-extracted basis functions for efficient analysis of scattering from electrically large targets," *Proc. IEEE*, vol. 101, no. 2, pp. 401–413, Feb. 2013.

[29] J. Fang, *Ray-Based Finite Element Method for High-frequency Helmholtz Equations*. Irvine, CA, USA: Univ. California, Irvine, 2017.

[30] J. Fang, J. Qian, L. Zepeda-Núñez, and H. Zhao, "Learning dominant wave directions for plane wave methods for high-frequency Helmholtz equations," *Res. Math. Sci.*, vol. 4, no. 1, pp. 1–35, Dec. 2017.

[31] T. S. A. Yeung, K. C. Cheung, E. T. Chung, S. Fu, and J. Qian, "Learning rays via deep neural network in a ray-based IPDG method for high-frequency Helmholtz equations in inhomogeneous media," *J. Comput. Phys.*, vol. 465, Sep. 2022, Art. no. 111380.

[32] D. Bouche, F. Molinet, and R. Mittra, *Asymptotic Methods in Electromagnetics*. Cham, Switzerland: Springer, 2012.

[33] J.-D. Benamou, "An introduction to Eulerian geometrical optics (1992–2002)," *J. Sci. Comput.*, vol. 19, pp. 63–93, Dec. 2003.

[34] O. P. Bruno and C. A. Geuzaine, "An $O(1)$ integration scheme for three-dimensional surface scattering problems," *J. Comput. Appl. Math.*, vol. 204, no. 2, pp. 463–476, 2007.

[35] C. P. Davis and W. C. Chew, "Frequency-independent scattering from a flat strip with TE_z-polarized fields," *IEEE Trans. Antennas Propag.*, vol. 56, no. 4, pp. 1008–1016, Apr. 2008.

[36] M. Zhuang, Q. Zhan, J. Zhou, Z. Guo, N. Liu, and Q. H. Liu, "A simple implementation of PML for second-order elastic wave equations," *Comput. Phys. Commun.*, vol. 246, Jan. 2020, Art. no. 106867.

[37] M. Giacomini, R. Sevilla, and A. Huerta, "Tutorial on Hybridizable Discontinuous Galerkin (HDG) formulation for incompressible flow problems," in *Modeling in Engineering Using Innovative Numerical Methods for Solids and Fluids*. Cham, Switzerland: Springer, 2020, pp. 163–201.

[38] N. C. Nguyen, J. Peraire, and B. Cockburn, "An implicit high-order hybridizable discontinuous Galerkin method for linear convection–diffusion equations," *J. Comput. Phys.*, vol. 228, no. 9, pp. 3232–3254, May 2009.

[39] R. M. Kirby, S. J. Sherwin, and B. Cockburn, "To CG or to HDG: A comparative study," *J. Sci. Comput.*, vol. 51, no. 1, pp. 183–212, Apr. 2012.

[40] J.-D. Benamou, F. Collino, and S. Marmorat, "Numerical microlocal analysis revisited," Ph.D. dissertation, INRIA, Centre de Recherche INRIA Paris-Rocquencourt, Rocquencourt, France, 2011.

[41] J.-D. Benamou, F. Collino, and O. Runborg, "Numerical microlocal analysis of harmonic wavefields," *J. Comput. Phys.*, vol. 199, no. 2, pp. 717–741, Sep. 2004.

[42] *Ray Optics Module User's Guide*, Version: September, COMSOL, Burlington, MA, USA, 2018, p. 77, vol. 10.

[43] G. Carluccio and M. Albani, "An efficient ray tracing algorithm for multiple straight wedge diffraction," *IEEE Trans. Antennas Propag.*, vol. 56, no. 11, pp. 3534–3542, Nov. 2008.

Haoqiang Feng (Graduate Student Member, IEEE) was born in Zhejiang, China, in 1997. He received the B.S. degree in information engineering from Zhejiang University, Hangzhou, Zhejiang, in 2019, where he is currently pursuing the Ph.D. degree in electronic science and technology.

His research interests include advanced numerical methods, multiphysics modeling, and high-performance computing.

Jianping Huang received the B.S. and Ph.D. degrees in geophysics from the University of Science and Technology of China, Hefei, China, in 2003 and 2008, respectively.

He is currently a Professor with the Department of Geophysics, China University of Petroleum (East China), Qingdao, China. He has published over 260 journal articles, including 136 SCI articles, and the H-index is 28. His research interests include seismic wave forward propagation and imaging.

Caipin Li was born in Fujian, China. He received the bachelor's degree in computer science and technology from Air Force Engineering University, Xi'an, China, in 2007, and the M.S. degree in communication and information systems from China Academy of Space Technology, Beijing, China, in 2010.

Since 2010, he has been with China Academy of Space Technology. He is currently a Professor of Satellite Payloads Engineering with China Academy of Space Technology, Xi'an, China. He has published around 40 articles and applied over 30 patents. His research interests include spaceborne radar systems, new radar system design, and SAR imaging processing.

Kang Liu was born in Siyang, China, in 1990. He received the B.S. degree in information engineering from Nanjing University of Aeronautics and Astronautics, Nanjing, China, in 2012, and the M.S. and Ph.D. degrees in information and communication engineering from the National University of Defense Technology, Changsha, China, in 2014 and 2017, respectively.

He is currently a Professor with the College of Electronic Science and Technology, National University of Defense Technology. His research interests include radar imaging and vortex electromagnetic wave technology.

Yi-Yao Wang (Graduate Student Member, IEEE) received the B.S. degree in information engineering from the College of Information Science and Electronic Engineering, Zhejiang University, Hangzhou, China, in 2021, where he is currently pursuing the Eng.D. degree in electronic science and technology.

His research interests include multiphysics modeling, high-performance electromagnetic computing, and matrix-free finite-element methods.

Wei E. I. Sha (Senior Member, IEEE) received the B.S. and Ph.D. degrees in electronic engineering from Anhui University, Hefei, China, in 2003 and 2008, respectively.

From July 2008 to July 2017, he was a Post-Doctoral Research Fellow and then a Research Assistant Professor with the Department of Electrical and Electronic Engineering, The University of Hong Kong, Hong Kong. From March 2018 to March 2019, he worked with University College London, London, U.K., as a Marie-Curie Individual Fellow. In October 2017, he joined the College of Information Science and Electronic Engineering, Zhejiang University, Hangzhou, China, where he is currently an Associate Professor. He has authored or co-authored 170 refereed journal articles, 140 conference publications (including three keynote talks, one short course, and 36 invited talks), eight book chapters, and two books. His Google Scholar citation is 7400 with an H-index of 43. His research involves fundamental and applied aspects in computational and applied electromagnetics, nonlinear and quantum electromagnetics, micro- and nano-optics, optoelectronic device simulation, and multiphysics modeling. His research interests include theoretical and computational research in electromagnetics and optics, focusing on the multiphysics and interdisciplinary research.

Qiwei Zhan (Member, IEEE) received the B.S. degree from the University of Science and Technology of China, Hefei, China, in 2013, and the M.S. degree in civil and environmental engineering and the Ph.D. degree in electrical and computer engineering from Duke University, Durham, NC, USA, in 2016 and 2019, respectively.

From June 2019 to August 2020, he was a Peter O'Donnell, Jr. Post-Doctoral Fellow with Oden Institute for Computational Engineering and Sciences, The University of Texas at Austin, Austin, TX, USA. Since September 2020, he has been with the College of Information Science and Electronic Engineering, Zhejiang University, Hangzhou, China, as a tenure-track Professor and a Ph.D. Supervisor. His research interests include multiphysics modeling, computational electromagnetics, computational mechanical waves, uncertainty quantification, effective medium theory, inverse problems, data assimilation, and scientific machine learning.